

# Catalysis Science & Technology

Accepted Manuscript



This is an *Accepted Manuscript*, which has been through the Royal Society of Chemistry peer review process and has been accepted for publication.

*Accepted Manuscripts* are published online shortly after acceptance, before technical editing, formatting and proof reading. Using this free service, authors can make their results available to the community, in citable form, before we publish the edited article. We will replace this *Accepted Manuscript* with the edited and formatted *Advance Article* as soon as it is available.

You can find more information about *Accepted Manuscripts* in the [Information for Authors](#).

Please note that technical editing may introduce minor changes to the text and/or graphics, which may alter content. The journal's standard [Terms & Conditions](#) and the [Ethical guidelines](#) still apply. In no event shall the Royal Society of Chemistry be held responsible for any errors or omissions in this *Accepted Manuscript* or any consequences arising from the use of any information it contains.



Journal Name

ARTICLE

## Atomistic Understanding on the Origin of High Oxygen Reduction Electro-catalytic Activity of Cuboctahedral Pt<sub>3</sub>Co-Pt Core-Shell Nanoparticles

Received 00th January 20xx,  
Accepted 00th January 20xx

DOI: 10.1039/x0xx00000x

www.rsc.org/

Guangzhi Hu<sup>a,c,†</sup>, Eduardo Gracia-Espino<sup>a,†,\*</sup>, Robin Sandström<sup>a</sup>, Tiva. Sharifi<sup>a</sup>, Shaodong Cheng<sup>b</sup>, Hangjia Shen<sup>c</sup>, Chuanyi Wang<sup>c</sup>, Shaojun Guo<sup>d</sup>, Guang Yang<sup>b,\*</sup>, Thomas Wågberg<sup>a,\*</sup>

PtM-based core-shell nanoparticles are a new class of active and stable nanocatalysts to promote oxygen reduction reaction (ORR), however, the understanding at atomistic level of their high electrocatalytic performance for ORR is still a great challenge. Herein, we report a synthesis of highly ordered, and homogeneous truncated cuboctahedral Pt<sub>3</sub>Co-Pt core-shell nanoparticles (cs-Pt<sub>3</sub>Co). By combining atomic resolution electron microscopy, X-ray photoelectron spectroscopy, extensive first-principles calculations, and many other characterization techniques, we conclude that the cs-Pt<sub>3</sub>Co nanoparticles are composed of a complete or nearly complete Pt monolayer skin, followed by a secondary shell containing 5-6 layers with a ~78 At% of Pt, in a Pt<sub>3</sub>Co configuration, and finally a Co rich core with 64 At% of Pt. Only this particular structure is consistent with the very high electrocatalytic activity of cs-Pt<sub>3</sub>Co nanoparticles for ORR, which is about 6 times higher than commercial 30%-Pt/Vulcan, and 5 times more active than non-faceted (spherical) alloy Pt<sub>3</sub>Co nanoparticles. Our study gives an important insight into the atomistic design and understanding of advanced bimetallic nanoparticles for ORR catalysis and other important industrial catalytic applications.

### Introduction

The oxygen reduction reaction is one of the most important technological catalytic reaction. It is a sluggish, rate limiting reaction that takes place at the cathode side in proton exchange membrane fuel cells, and therefore the development of efficient catalysts with long-term stability represent a key issue to make the society less fossil dependent.<sup>1, 2</sup> The last decade the studies and development of new advanced catalyst has merely exploded, and a large reason is due to strong advances in materials science and

nanotechnology.<sup>3, 4, 5-8</sup> The aim in most of these studies is to replace the expensive and scarce Pt (37 ppb in earth crust,<sup>9</sup> with a current price of more than 1000 US dollar per troy ounce), with a less expensive but yet more efficient catalyst, which ideally shows endurance to catalyst poisoning, such as carbon monoxide; a common impurity in steam reformed hydrogen. Remarkable improvement on ORR performance has been achieved by rational design of nanocatalyst supported on carbon nanostructures,<sup>10-12</sup> in particular by manufacturing alloys of Pt and transition metals, in ratios Pt<sub>3</sub>M (M denotes a transition metal).<sup>13-15</sup> A well-studied example is the Pt<sub>3</sub>Ni structure,<sup>16, 17</sup> The reason for an enhanced ORR efficiency has been explained in various ways, such as a shift of the *d*-band center of the transition metal alloy, or by a lattice strain imposed on the noble metal lattice.<sup>18, 19</sup> The main consequence, however seems to be that the vicinity of a suitable amount of transition metal atoms close to the noble metal atoms raises the oxygen adsorption energy, lowers the energy barrier for O<sub>2</sub> dissociation and lowers the adsorption of intermediate species O\*.<sup>20</sup> All these effects positively influences the ORR efficiency and results in a lower overpotential of the catalyst. To tune the positive effects of transition metals on the noble metals, several groups have further advanced the nanoparticle design and synthesized so called PtM-Pt core-shell nanoparticles comprising a transition metal core and Pt-skin shell,<sup>17, 21</sup> exhibiting a remarkable catalytic activity

<sup>a</sup> Department of Physics, Umeå University, 901 87 Umeå, Sweden.

<sup>b</sup> Electronic Materials Research Laboratory, Key Laboratory of the Ministry of Education and International Center for Dielectric Research, Xi'an Jiaotong University, Xi'an 710049, China

<sup>c</sup> Laboratory of Environmental Science and Technology, The Xinjiang Technical Institute of Physics and Chemistry, Chinese Academy of Sciences, Urumqi 830011, China

<sup>d</sup> Physical Chemistry and Applied Spectroscopy, Los Alamos National Laboratory, Los Alamos, New Mexico 87545 U. S. A.

\*Correspondence should be addressed to Thomas Wågberg (Thomas.wagberg@physics.umu.se), Guang Yang (g.yang@mail.xjtu.edu.cn) or Eduardo Gracia-Espino (Eduardo.gracia@physics.umu.se).

Electronic Supplementary Information (ESI) available: [High-resolution XPS, EDS, and TGA analysis. TEM micrographs and particle size distribution. Molecular models used in DFT]. See DOI: 10.1039/x0xx00000x

for ORR. However, a full understanding on the mechanisms behind an efficient ORR process based on PtM-Pt core-shell nanoparticle, and a true insight in how the catalytic activity correlates with the exact structure of the nanoscale PtM-Pt core-shell catalyst is lacking. Also, studies which combine theoretical data with extensive experimental data on well-defined core-shell nanoparticle systems are scarce. Here we report a detailed theoretical and experimental case study of highly homogeneous well-ordered truncated cuboctahedral Pt<sub>3</sub>Co-Pt core-shell nanoparticles (cs-Pt<sub>3</sub>Co), and compared them with non-faceted (spherical) alloy Pt<sub>3</sub>Co nanoparticles to better understand why core-shell nanoparticles are extremely active for ORR from an atomic view point. The STEM mapping results show that the exact structure of cs-Pt<sub>3</sub>Co nanoparticles are composed of a complete or nearly complete Pt monolayer skin, followed by a secondary shell containing 5-6 layers with a ~78 At% of Pt, in a Pt<sub>3</sub>Co configuration, and a Co rich core with 64 At% of Pt, making them exhibit more than six-fold increase in ORR catalytic activity and a positive shift of the polarization half-wave potential of 63 mV (best electrodes display shifts of more than 80 mV) compared to commercial Pt/Vulcan. Density functional theory (DFT) computations further show that the high catalytic activity of cs-Pt<sub>3</sub>Co nanoparticles cannot be explained by considering a complete segregation of Pt and Co, forming a pure Pt-shell and a Co-core, but rather by a presence of Co-atoms also in the outer layers, forming the so-called Pt-skeleton structure.<sup>22</sup> Here we also point out, that our theoretical data reveals that the catalytic efficiency of this type of core-shell particles, gradually increases with number of shell-layers with a maximum efficiency at 5-6 layers. Our study gives fundamental insight into the design and properties of advanced catalyst nanoparticles, which is of both scientific and technological importance.

## Experimental section

### Synthesis of catalyst composites

The cs-Pt<sub>3</sub>Co nanocrystals were prepared by mixing Pt(II) acetylacetonate (Pt(acac)<sub>2</sub>) with Cobalt(III) acetylacetonate (Co(acac)<sub>3</sub>) in N,N-dimethylformamide (DMF), and then the solution is transferred into a quartz tube inner-lined stainless autoclave, where the mixture is treated at 140 °C for 24 hours. As reference samples we prepared a non-faceted (spherical) Pt<sub>3</sub>Co, labelled sp-Pt<sub>3</sub>Co, by a thermal annealing method at 700 °C in a mixture of 5% hydrogen + 95% argon atmosphere with a heating rate about 5 °C/min for 2 hours. The latter method is well-known to not give rise to faceted core-shell particles, but rather homogenous spherical Pt<sub>3</sub>Co alloy particles. As a second reference sample, a commercial Pt/Vulcan sample was used (Pt loading 60%, Premetek, US), labelled Pt/Vulcan. The loading of all samples were determined by Thermal gravimetric analysis (TGA) on a Mettler Toledo TGA/DSC 1LF/948.

### Characterization

Transmission electron microscopy (TEM) analysis was performed on a JEOL 2100 microscope operated at 200 kV. The atomic resolution high angle annular dark field (HAADF) scanning transmission electron microscopy (STEM) images and energy dispersive x-ray spectroscopy (EDS) analyses were obtained from a JEOL ARM200F microscope equipped with probe Cs corrector.

XPS spectra were recorded with Axis Ultra DLD electron spectrometer (Kratos Analytical LTD, UK). A monochromated Al K<sub>α</sub> source operated at 150 W and a hybrid lens system with a magnetic lens, providing an analysis area of 0.3 mm x 0.7 mm, were used for the measurements. Before the measurements, calibration of the binding energy (BE) scale was made by the ISO/TC 201 Standard:

ISO 15472:2010 – “X-ray photoelectron spectrometers -- Calibration of energy scales”, using corresponding photoelectron lines of Au 4f<sub>7/2</sub> (at 83.96 eV), Ag 3d<sub>5/2</sub> (at 368.21 eV) and Cu 2p<sub>3/2</sub> (at 932.62 eV). Due to a good conductivity of the samples, a charge neutralization system was not used, and experimentally measured binding energies did not require an additional calibration.

The cyclic voltammetry tests were performed in 0.1 M HClO<sub>4</sub>. The different samples were re-dispersed in the mixture of deionized water and isopropanol solution containing 0.05% Nafion to get a suspension with catalyst concentration about 5 mg/mL. Prior to each electrochemical testing, the glassy carbon electrode (diameter 5 mm) was carefully polished with 0.05 mm aluminum oxide powder and then cleaned by ultrasonication in acetone, ethanol and water, respectively. 5 μL portions of the suspensions were individually cast on the glassy carbon disk electrode (GCE, 5 mm in diameter) and then dried under room temperature. Cyclic voltammetry (CV) and rotating electrode (RDE) tests were recorded on an Autolab PGSTAT-302N potentiostat/galvanostat connected to a rotating electrode system (Pine, US) with Ag/AgCl as the reference electrode and a platinum rod as the counter electrode. The working electrode was scanned in 0.1 M HClO<sub>4</sub> solution by successive voltammetry (CV) and line sweep voltammetry (LSV) at 0.05 V/s in the potential region 0.05-1.05 V. Prior to CV and RDE tests, the electrolyte solution was bubbled with oxygen or argon for more than 30 min with a flowing rate of 100 ml/min. The current densities in both CV and RDE data were normalized according to the geometric area of the glassy carbon disc. Before the CO stripping experiments the catalyst electrode was bubbled with CO for 15 min under -0.178 V (vs. Ag/AgCl) and then bubbled with argon for another 15 min to remove the dissolved CO in the electrolyte.

### Computational Details

First principles calculations were performed within the framework of the density functional theory<sup>23</sup> using the generalized gradient approximation and the revised Perdew, Burke and Ernzerhof (RPBE)<sup>24</sup> as the exchange-correlation term. The wave functions for the valence electrons are represented by a linear combination of pseudo-atomic numerical orbitals<sup>25</sup> using double- $\zeta$  plus one polarized orbital basis. A 10×10×1 Monkhorst-Pack<sup>26</sup> grid is used to sample the Brillouin zone. A Methfessel-Paxton<sup>27</sup> smearing of 0.1 eV and a Pulay mixing is employed to aid convergence on the self-consistent electron density. The real-space grid used for charge and potential integration is equivalent to a plane wave cut-off energy of 400 Ry, and both the total energy and atomic forces were corrected by a self-consistent dipole correction. The periodically repeated slabs are separated by at least 8 vacuum layers to avoid self-interactions. Four different metal slabs are used as model to study the ORR. The first system is represented by (2×2) Pt(111) slab over a cobalt core. The second one is represented by (2×2) Pt-skin over a Pt<sub>3</sub>Co(111) slabs also over a cobalt core, forming a Pt-skeleton structure. The third system is a (2×2) pure Pt<sub>3</sub>Co(111) surface (without the Pt skin layer), and finally, a pure (2×2) Pt(111) surface is used as a reference system. The adsorption energies of intermediates are calculated using slabs consisting of 4 to 9 layers, where the bottom 3 layers belonging to the cobalt core are kept fixed during all calculations, while the remaining layers are Pt or Pt<sub>3</sub>Co based. On all surfaces, the oxygen is chemisorbed on a hollow face-centered cubic (fcc) site. The adsorbates and all the Pt or Pt<sub>3</sub>Co slabs are allowed to relax freely until the maximum forces were <0.04 eV/Å. The DFT computations were performed using the SIESTA code,<sup>28</sup> and the simulated TEM image was obtained using the multislice approach as described by Gómez-Rodríguez, *et al.*<sup>29</sup>

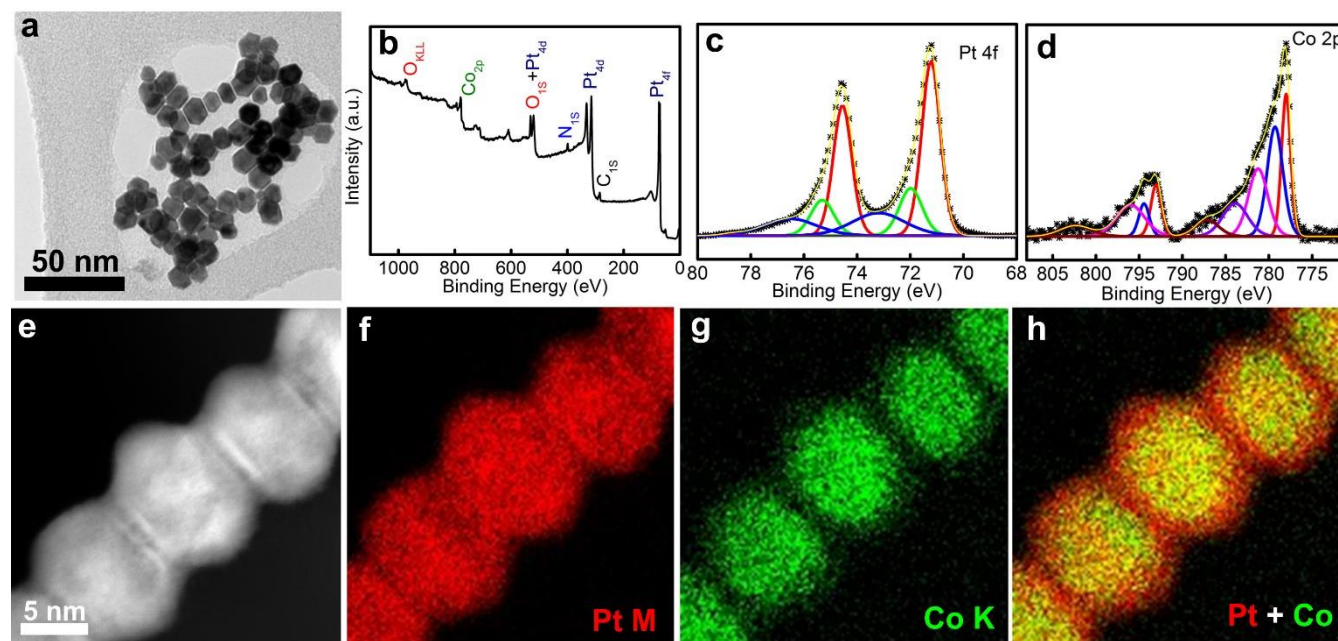


Figure 1. (a) TEM image of cuboctahedral  $cs\text{-Pt}_3\text{Co}$ . (b) Overall XPS curve of  $cs\text{-Pt}_3\text{Co}$  nanocrystals and the corresponding high resolution XPS curves of Pt 4f (c) and Co 2p (d). (e) HAADF STEM image for EDS mapping of  $cs\text{-Pt}_3\text{Co}$  cuboctahedrons. (f-g) EDS mapping with signals attributed to Pt and Co, respectively. (h) Overlap of Pt and Co EDS signals.

The free energy of intermediates is calculated based on the computational hydrogen-electrode (CHE) model.<sup>1</sup> The CHE model has been used in several publications proving their feasibility to study electrochemical reactions. The CHE model defines that at standard conditions (pH = 0 in the electrolyte and 1 bar of  $\text{H}_2$  in the gas phase at 298.15 K the chemical potential of a proton-electron pair ( $\text{H}^+ + \text{e}^-$ ) in solution is equal to half of the chemical potential of a gas-phase  $\text{H}_2$  molecule. The Gibbs free energy change ( $\Delta G_0$ ) of intermediates is calculated by  $\Delta G_0 = \Delta E + \Delta \text{ZPE} - T\Delta S$ , where  $\Delta E$  is the energy change obtained from DFT calculations,  $\Delta \text{ZPE}$  is the change in zero-point energies,  $T$  is temperature (298.15 K), and  $\Delta S$  is the change in entropy. Standard values of zero-point energies and entropies for the ORR intermediates are obtained from Norskov, *et al.*<sup>1</sup> The effect of a bias on states involving electrons transfer results in a direct shift in the free energy of the electrons, and it can be included by correcting the Gibbs free energy ( $\Delta G_U$ ) by  $-eU$ , where  $U$  is the applied bias and  $e$  is the number of electrons transferred. Therefore computing the adsorption energies of the intermediates in the ORR makes possible to calculate the overall free energy pathway as a function of the applied bias, thus the total change in free energy is given by  $\Delta G = \Delta G_0 + \Delta G_U$ .

## Results and Discussion

The solvothermal synthesis of the  $cs\text{-Pt}_3\text{Co}$  nanoparticles was obtained by using DMF as solvent, which has been shown to both work as stabilizer and reducing agent for the formation of Pt-Co bimetallic systems.<sup>30</sup> Figure 1a shows a TEM image of the unsupported  $cs\text{-Pt}_3\text{Co}$  nanoparticles. It is found that all

nanoparticles exhibit a structure consistent with truncated cuboctahedrally shaped nanoparticles with a narrow size distribution of  $11.3 \pm 1.8$  nm (Figure S1). X-ray photoelectron spectroscopy (XPS) of  $cs\text{-Pt}_3\text{Co}$  in Figure 1b reveals that the nanoparticles are composed of C, O, N, Co and Pt, where the C, N and part of the O can be assigned to residual solvent, and other agents adsorbed on the catalyst surface after the washing procedures. This assignment is particularly clear by investigating the high-resolution XPS spectrum (see supporting Figure S2) of C, displaying clear signals of C-C, C-N and C-O that can be ascribed to acetylene-acetone and DMF adsorbed on the catalyst. Figure 1c and 1d, display the high-resolution XPS Pt 4f and the Co 2p spectrum, respectively and indicates a metallic character of the Pt atoms in the  $cs\text{-Pt}_3\text{Co}$  nanocrystals while both oxidized and metallic states are found for the Co atoms. From the XPS data, we measure a Pt/Co ratio of 4.75, which is considerably larger than the ratio obtained from energy dispersive X-ray spectrometry (EDS) measurements (Pt/Co = 3.2, see below). Since XPS is a surface sensitive technique, probing approximately the upper 2 nm of the particles, this difference indicates Pt-rich surfaces, being possible a core-shell structure of a  $\text{Pt}_3\text{Co}$  alloy. The core-shell structure is further supported by HAADF images and EDS mapping. Figure 1e shows the HAADF image of the  $cs\text{-Pt}_3\text{Co}$  nanoparticles, arranged in a “necklace” configuration, which is frequently observed for unsupported  $\text{Pt}_3\text{Co}$  bimetallic nanocrystals. From the elemental signals of Pt and Co shown in Figure 1f and 1g, it is clear that while the Pt signal (red) is distributed over the “full size” of the nanoparticles, the Co signal (green) is concentrated in the core of

the particle, with only weak signals of Co in the shell. This is even clearer from the overlay image shown in Figure 1h, where the combination of the red Pt signal and the green Co signal yields a yellow signal which is very strong in the core of the nanoparticles. The resulting Pt/Co atomic ratio is equal to 3.2 measured for four individual cs-Pt<sub>3</sub>Co nanoparticles (see supplementary Figure S4).

Figure 2a-b shows the high resolution HAADF images of individual cs-Pt<sub>3</sub>Co nanocrystals. From the micrographs, two important characteristics of the cs-Pt<sub>3</sub>Co can be concluded; i) their structure is clearly compatible with truncated cuboctahedrons. This is particularly obvious by the atomic model of a truncated cuboctahedron with hexagonal faces depicted in Figure 2c and its corresponding simulated image in Figure 2d, which perfectly matches those in figure 2a-b, ii) the core-shell structure is easily observed from all particles in Figure 2a-b, by a clear contrast between the outer 5-6 layers and the core part of the particle, however the detailed shell and core composition are difficult to estimate. At higher resolution the sharp contrast is even more pronounced (Figure 2b). From the HAADF-STEM image of the individual cs-Pt<sub>3</sub>Co nanocrystals we measure a distance between atoms in the outer layers of 0.226 nm, which agrees well with the Pt-Pt atom distance in pure Pt nanoparticles. In the core, we can deduce a slightly reduced lattice distance of 0.206 nm, which most likely can be rationalized by a higher fraction of Co in the Pt-Co structure which should lead to a lowering of the lattice distance. This is in good agreement with the powder X-ray diffraction of cs-Pt<sub>3</sub>Co shown in supporting Figure S3, which exhibits three main peaks at 40.6, 47.2 and 68.8 degrees, assigned to diffraction from the (111), (200) and (220) crystal planes of the face centered cubic structure. These are slightly "down shifted" by 0.15, 0.2 and 0.5 degrees compared to the peak positions of the intermetallic Pt<sub>3</sub>Co reflections (PDF-#-04-004-5243).

To derive the nanostructure and in particular the core-shell configuration, we performed EDS line scans to individual cs-Pt<sub>3</sub>Co particles. An example of a line-scan is depicted in Figure 2e, and the corresponding intensity profiles of Pt and Co components are displayed in Figure 2f. From these data we can conclude that the shell indeed is very rich on Pt, especially in the outer layers, where almost no signal of Co is detected.

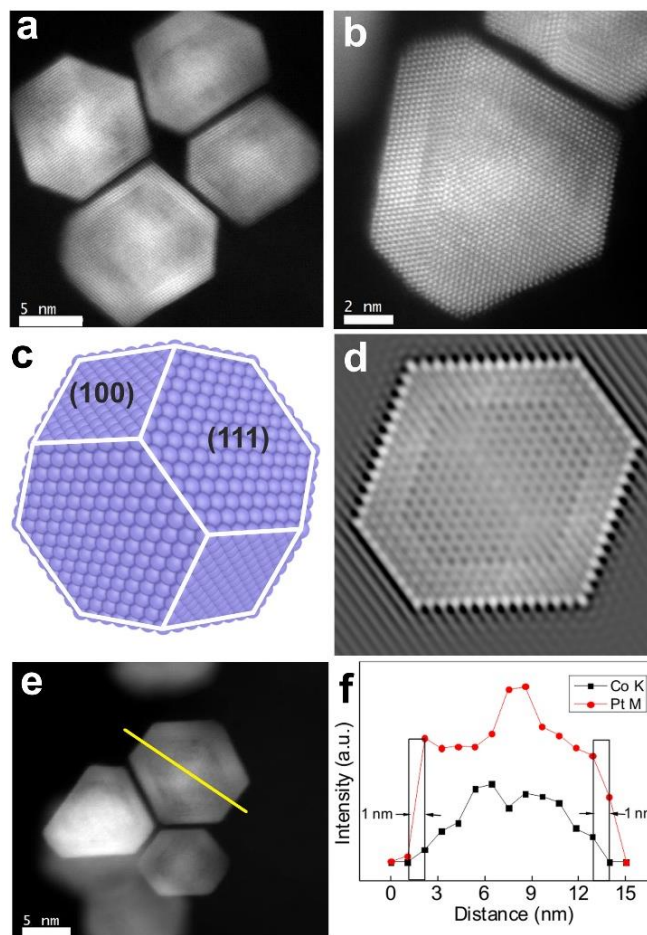


Figure 2. (a) High-angle annular dark-field scanning transmission electron microscopy (HAADF-STEM) image of the as-prepared cuboctahedral Pt<sub>3</sub>Co nanoparticles. (b) Atom-resolution HAADF-STEM image of a core-shell Pt<sub>3</sub>Co cuboctahedral nanocrystal. (c) Atomic model of a cuboctahedral core-shell (cs-Pt<sub>3</sub>Co) nanoparticle, and (d) its corresponding image simulation. (e) HAADF-STEM image of Pt<sub>3</sub>Co core-shell particles and the (f) intensity profiles of Pt and Co components in one single nanoparticle obtained by a EDS line scan analysis along the yellow line in shown in (e) from left to right.

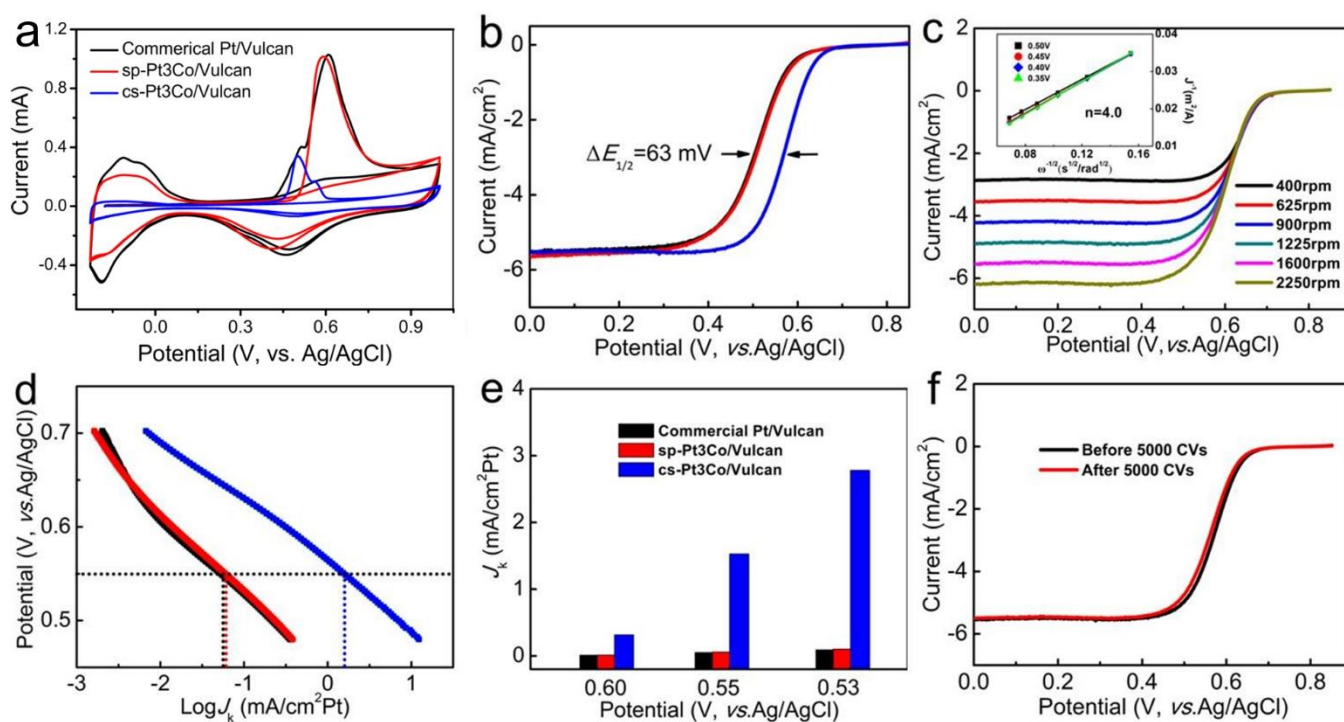


Figure 3. (a) CO stripping curves of commercial Pt/Vulcan, sp-Pt<sub>3</sub>Co/Vulcan and cs-Pt<sub>3</sub>Co/Vulcan in argon saturated 0.1 M HClO<sub>4</sub> solution with scanning rate 0.05 V/s. (b) The polarized curves of the catalyst electrode (Pt/Vulcan as black line, sp-Pt<sub>3</sub>Co/Vulcan as red line and cs-Pt<sub>3</sub>Co/Vulcan as blue line) in O<sub>2</sub> saturated 0.1 M HClO<sub>4</sub> solution at a scan rate of 0.01 V/s with the rotating speed of 1600 rpm; (c) The polarized curves of the cs-Pt<sub>3</sub>Co/Vulcan catalyst electrode at different rotating speed ranging from 400 to 2025 rpm in 0.1 M HClO<sub>4</sub> solution at a scan rate of 10 mV/s. the inset is the Koutecky–Levich plots from ORR data for cs-Pt<sub>3</sub>Co/Vulcan electrode at different potentials; (d) Comparison of specific activities ( $j_k$ ) for commercial Pt/Vulcan (black), sp-Pt<sub>3</sub>Co/Vulcan (red) and cs-Pt<sub>3</sub>Co/Vulcan (blue); (e) comparison of normalized activities of the three catalysts at different potentials; (f) Polarized curves of cs-Pt<sub>3</sub>Co/Vulcan catalyst for ORR before and after 5000 potential cycles at a rotating speed of 1600 rpm.

The EDS line scan thus give unambiguous support to the conclusions made from the EDS mapping and the HAADF images, namely that the cs-Pt<sub>3</sub>Co are composed of a Pt-rich shell, and that the inner atomic layers gradually have an increased Co content, until a Co-rich core is reached.

Now, it is possible to estimate the amount of Pt at the inner layers of the nanoparticle. Considering a ~11 nm truncated cuboctahedral Pt<sub>3</sub>Co nanoparticle with an overall Pt/Co ratio of 3.2 (as obtained by EDS, supporting Figure S4), that is composed by 21 atomic shells, and that the outer 6 layers are Pt-rich, with a Pt/Co of 4.75 (as indicated by XPS). We estimate that the 15 core layers (since the first 6 are considered to be part of the shell) exhibit an inner Pt/Co ratio ~1.8, and that the shell might exhibit a transition region (~5 layers) with a Pt/Co = 3.5. We point out that this is an “indirect” estimation based on a combination of the experimental results (EDS and XPS) and theoretical simulations. A more detailed explanation for this estimation is given in supporting information (Figure S5, and related discussion).

To test the catalytic activity for oxygen reduction and understand how the exact structure of bimetallic nanoparticles correlates with the catalytic activity, we performed extensive electrochemical tests. As reference samples for our electrochemical tests, we use two other materials; 1) commercial 30% Pt/Vulcan (Pt/Vulcan) and 2) spherical Pt<sub>3</sub>Co/Vulcan (sp-Pt<sub>3</sub>Co/Vulcan) catalysts. The non-faceted 3.0 nm sp-Pt<sub>3</sub>Co NPs/Vulcan was synthesized by a different methodology (see the details in supporting information). Figure S6 show that they are also well distributed, and crystalline, but with no distinct crystal shape. Figure S7 shows the cyclic voltammograms (CVs) of the three different electrodes (Pt/Vulcan, sp-Pt<sub>3</sub>Co/Vulcan and the cs-Pt<sub>3</sub>Co/Vulcan (30 % loading)) in argon-saturated 0.1 M HClO<sub>4</sub>, and displays the hydrogen under potential formation/stripping which appears at potential lower than 0.1 V (v.s. Ag/AgCl).<sup>31</sup> It is obvious that hydrogen ad- and desorption area of commercial Pt and sp-Pt<sub>3</sub>Co nanocatalyst is much higher than that of cs-Pt<sub>3</sub>Co catalyst. This is because the size of cs-Pt<sub>3</sub>Co nanoparticle is much larger than that of the commercial Pt/Vulcan and sp-Pt<sub>3</sub>Co. The electrochemical active surface area (EASA) was

calculated and corrected by CO sweeping voltammetry to 6.33 cm<sup>2</sup> for Pt/Vulcan, 6.15 cm<sup>2</sup> for sp-Pt<sub>3</sub>Co/Vulcan and 1.36 cm<sup>2</sup> for cs-Pt<sub>3</sub>Co/Vulcan (figure 3a).

Before the ORR activity tests, all catalyst electrodes were electrochemically activated by cycling the potential between -0.2 and 0.8 V with a sweep rate of 50 mV/s for 50 cycles in argon-saturated electrolyte solution and Ag/AgCl as reference electrode. The polarization curves for the three catalyst electrodes in O<sub>2</sub>-saturated 0.1 M HClO<sub>4</sub> solution at 1600 r.p.m is shown in Figure 3b. It is clear that the half-wave potential of cs-Pt<sub>3</sub>Co/Vulcan (0.57 V) is much higher than that of sp-Pt<sub>3</sub>Co/Vulcan (0.51 V) and commercial Pt/Vulcan catalyst (0.51 V), manifesting a significantly better electrocatalytic activity toward ORR of cs-Pt<sub>3</sub>Co/Vulcan than both sp-Pt<sub>3</sub>Co/Vulcan and Pt/Vulcan catalysts. Performing similar tests for six corresponding sets of electrodes show a positive shift of the polarization half-wave potential of 63 mV compared to commercial Pt/Vulcan. The electron transfer number (*n*) of ORR for the cs-Pt<sub>3</sub>Co catalyst electrode was calculated by the ORR polarization curves at different rotating speed according to the Koutecky–Levich theory expressed by<sup>32, 33</sup>

$$\frac{1}{J} = \frac{1}{J_d} + \frac{1}{J_k} \quad (1)$$

$$J_d = 0.62nFAC_{O_2}D^{2/3}\nu^{-1/6}\omega^{1/2} \quad (2)$$

Where *J* is the measured current, *J<sub>d</sub>* the diffusion limited current, and *J<sub>k</sub>* is the kinetic current. *n* is the number of electrons transferred; *F* is Faraday's constant; *A* is the area of the electrode; *D* is the diffusion coefficient of O<sub>2</sub> in 0.1 M HClO<sub>4</sub> solution; *ν* is the kinematic viscosity of the electrolyte; *ω* is the angular frequency of rotation speed and *C<sub>O2</sub>* is the concentration of molecular oxygen in 0.1 M HClO<sub>4</sub> solution. From equations (1) and (2), *n* is equal to 4.0 for cs-Pt<sub>3</sub>Co/Vulcan (Figure 3c inset). The specific activity of the three electrocatalysts was also compared by mean of the kinetic current (*J<sub>k</sub>*) at the potential window from 0.5 to 0.7 V (vs. Ag/AgCl) as shown in Figure 3d. The specific activity at 0.55 V, normalized by the surface activity area of cs-Pt<sub>3</sub>Co is 1.44 mA/cm<sup>2</sup> Pt, which is six times higher than that of Pt-Vulcan catalyst (0.22 mA/cm<sup>2</sup>) and five times higher than that of sp-Pt<sub>3</sub>Co (0.24 mA/cm<sup>2</sup>), indicating a superiority of cs-Pt<sub>3</sub>Co catalyst towards ORR. Durability tests were also performed by cycling at the potential window between 0.6 and 1.0 V (vs. Ag/AgCl) in O<sub>2</sub>-saturated 0.1 M HClO<sub>4</sub> at a scan rate of 200 mV/s. Figure 2d shows the ORR polarization curves for the core-shell Pt<sub>3</sub>Co/Vulcan before and after 5000 potential sweeps, demonstrating a 11 mV negative shift in ORR polarization half-wave potential after the potential sweeps, suggesting a good stability of the as prepared cs-Pt<sub>3</sub>Co catalysts. Corresponding tests for the sp-Pt<sub>3</sub>Co/Vulcan and the Pt/Vulcan catalysts show an undesirable shift of 35, and 54 mV respectively (Figure S9, and S10). Meanwhile there is no observable change in morphology for cs-Pt<sub>3</sub>Co after the durability test (Figure S11). A detailed comparison with previously reported results for similar catalysts and under similar conditions is given in table S5 in supporting information.

We thoroughly described the core-shell structure of the cs-Pt<sub>3</sub>Co cuboctahedral nanoparticles and showed their advantageous properties for ORR activity. Even by our extensive XPS, EDS, and HRTEM characterization, the shell composition is however difficult to estimate unambiguously. Thus, we now use DFT to elucidate if the shell is made of pure Pt atoms, or as our hypothesis suggest, the shell exhibit a true Pt<sub>3</sub>Co composition, since both options may give rise to a similar core-shell contrast observed in HRTEM (Figure 1-2). We also use DFT to comprehend the correlation between the shell thickness and the electrocatalytic activity. However, before we

describe our results, it is important to point out that a pure homogeneous Pt<sub>3</sub>Co shell, where Co atoms are located at the surface, significantly limits the ORR activity, due to too strong binding of O\*, and OH\* intermediates by the Pt<sub>3</sub>Co structure (see table S4). A high ORR activity requires the presence of at least one monolayer of Pt at the surface. Such structure is referred as a skeleton-type structure by Stamenkovic, *et al.*<sup>17</sup>

We have built four different systems that will help us to elucidate the effects on the shell thickness and composition on the ORR performance. The first system, labeled cs-Pt-Co-*x*, is a core-shell structure where the outer layers are made of pure Pt (with *x* representing the number of Pt-layers) (Figure 4b and S12) and the inner core comprises only cobalt atoms. The cs-Pt-Co-*x* system is designed to keep the bulk lattice constant of pure platinum as obtained by DFT (4.02 Å), being in good agreement when compared with the experimental value of 3.92 Å.<sup>34</sup> The second configuration is denoted cs-Pt<sub>3</sub>Co-*x*. It is also a core-shell structure, where the outermost layer contains only Pt atoms, the rest of the shell is made of Pt<sub>3</sub>Co alloy (skeleton-type structure), and the inner core is again made of pure cobalt. The cs-Pt<sub>3</sub>Co-*x* configuration is shown in Figure 4c and Figure S13. In this case, the cs-Pt<sub>3</sub>Co-*x* system is fixed to the bulk lattice constant of Pt<sub>3</sub>Co alloy (3.91 Å, as obtained by DFT). The third and fourth configurations are a pure Pt<sub>3</sub>Co and a pure Pt slabs that are used just as reference systems. Detailed information can be found in computational section and supporting information.

The electrochemical ORR activity has been evaluated using the computational hydrogen electron model,<sup>1</sup> which has shown to accurately describe trends in electrocatalytic activity in diverse systems. We calculated the oxygen adsorption energy ( $\Delta E_O$ ) while modifying the number of shell layers for both cs-Pt-Co-*x* and cs-Pt<sub>3</sub>Co-*x* systems. These results are shown in Figure 4a. In both core-shell configurations, the oxygen adsorption is weakened (larger positive values) instantly by placing only a single-layer shell above the cobalt core. Here both systems are almost identical with a pure Pt shell above a Co-core, and only differs in the lattice parameter. Increasing the number of shell layers (see figure 4 b, and c) further increase the oxygen adsorption energy, until it reach a maximum, corresponding to their respective bulk components. In the case of cs-Pt-Co-*x* system, the maximum value is equivalent to a pure Pt(111),  $\Delta E_O = 1.59$  eV, in good agreement with previous reports,<sup>1</sup> while for the cs-Pt<sub>3</sub>Co-*x* systems, the maximum correspond to a bulk Pt-Pt<sub>3</sub>Co with an  $\Delta E_O = 1.82$  eV. It is important to note here that the Pt-Pt<sub>3</sub>Co system exhibit a skin of Pt, since without this the Pt<sub>3</sub>Co system is highly inefficient for oxygen reduction (see S3).

The change in adsorption energy can be attributed to two different phenomena, a substrate (core) and a strain effect.<sup>35, 36</sup> The substrate effect is mainly manifested by a shift of the *d*-band center of Pt as a consequence of the electronic contribution from the underlying Co atoms. This effect is directly observed in the cs-Pt-Co-*x* system with 1 to 3 Pt shell layers, where the *d*-band center is shifted towards more negative values, resulting in lower adsorption energy,<sup>17, 18</sup>  $\Delta E_O$ . Interestingly, it is clear that a Pt-shell thickness larger than three layers, loose completely the effect of electron charge transfer from the Co-core, meaning that surface atoms are not able to feel any effect from the core-atoms being more than three layers away. The strain effect is, on the other hand, observed in the cs-Pt<sub>3</sub>Co-*x* system, with *x* = 4-6, where the thick shell substantially decrease the substrate effect of the cobalt core observed when thickness is less than 4 layers, and instead the observed effect can mainly be attributed to the compressed Pt-skin

(due to the smaller lattice constant of Pt<sub>3</sub>Co compared to pure Pt). Other cs-Pt<sub>3</sub>Co-x systems with < 4 shell layers exhibit the contribution of both phenomena, resulting in weaker  $\Delta E_{\text{O}}$  and lower ORR activity. The results discussed above are presented in Figure 4d

which shows the  $\Delta E_{\text{O}}$  as function of the platinum *d*-band center with respect to the Fermi Level ( $\epsilon_{\text{d}} - \epsilon_{\text{F}}$ ), as

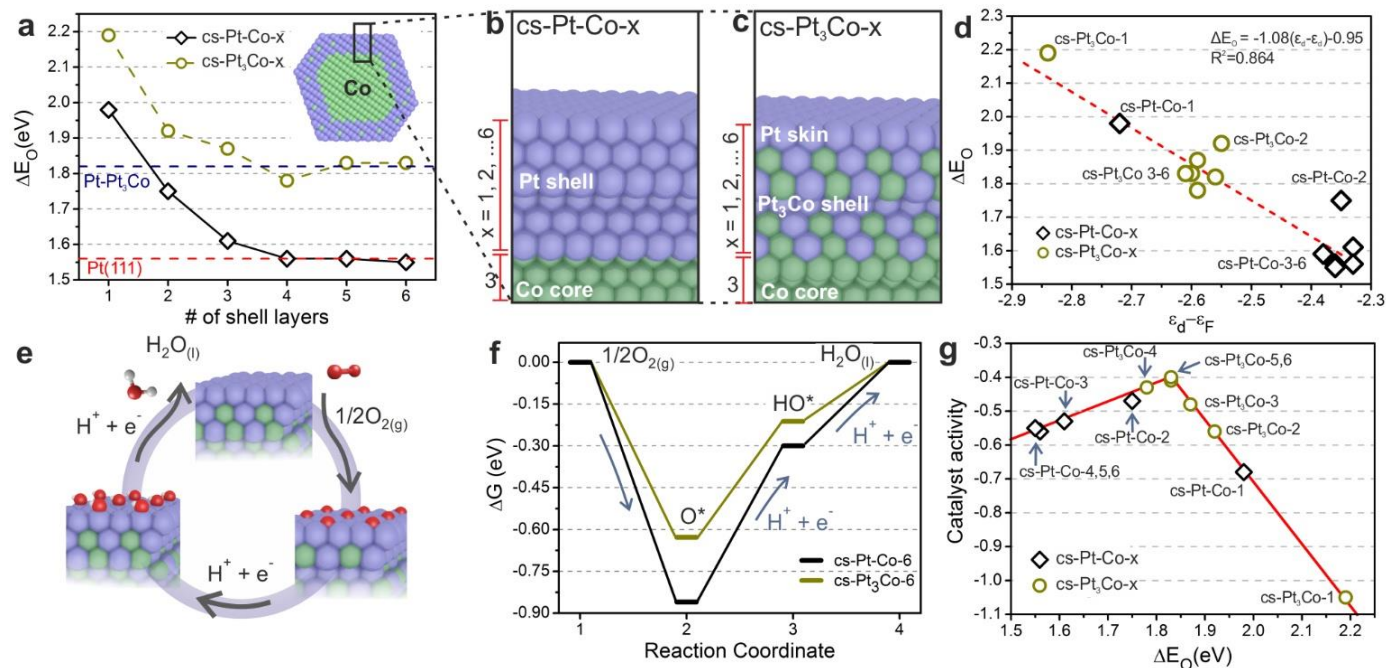


Figure 4. (a) Oxygen adsorption energy ( $\Delta E_{\text{O}}$ ) as a function of the number of shell layers. The dashed lines represent  $\Delta E_{\text{O}}$  value when pure Pt(111) (red) or pure Pt<sub>3</sub>Co(111) (blue) are used. The core-shell configurations of (b) cs-Pt-Co-x and (c) cs-Pt<sub>3</sub>Co-x systems, where the shell thickness varies from 1 up to 6 metal layers. (d)  $\Delta E_{\text{O}}$  as function of the *d*-band center ( $\epsilon_{\text{d}} - \epsilon_{\text{F}}$ ), the numbers next to the label indicates the shell thickness, and the line represents the linear fitting. (e) Schematic diagram of the ORR studied. (f) Free energy change during the ORR on cs-Pt-Co-6 and cs-Pt<sub>3</sub>Co-6 systems, where the smaller  $\Delta E_{\text{O}}$  on cs-Pt<sub>3</sub>Co-6 results in lower  $\eta_{\text{ORR}}$ . (g) Activity volcano plot for ORR as a function of  $\Delta E_{\text{O}}$  for the cs-Pt-Co-x and cs-Pt<sub>3</sub>Co-x systems at different surfaces thickness, the line is just a guide to the eyes.

an average of the Pt atoms at the outer layer). A linear relationship between  $\Delta E_{\text{O}}$  and  $\epsilon_{\text{d}} - \epsilon_{\text{F}}$  is in agreement with previous publications.<sup>18</sup>

To further evaluate the ORR performance of the different systems, we have studied the adsorption energies of O\* and HO\* intermediates for the ORR, as exemplified in Figure 4e. To obtain the oxygen reduction overpotential ( $\eta_{\text{ORR}}$ ), which is the single most important characteristics for the performance of the catalyst, we calculated the Gibbs free energy ( $\Delta G$ ) of the intermediates, as described in the computational methodology. Figure 4f shows the free energy diagram of cs-Pt-Co-6 and cs-Pt<sub>3</sub>Co-6 system (similar results are obtained for 4- and 5-layers shell systems). The significantly weaker adsorption energy of O\*,  $\Delta E_{\text{O}}$ , for cs-Pt<sub>3</sub>Co (~0.25 eV weaker than pure Pt(111)) results in lower  $\eta_{\text{ORR}}$  (0.41 V compared with 0.55 V for pure Pt). Norskov, *et al*<sup>1</sup> determined that Pt  $\eta_{\text{ORR}} = 0.48$  V, the difference might arise from the use of a localized orbital basis instead of a plane-wave approach used by Norskov, resulting in a slightly underestimation of the HO\* adsorption, increasing the Pt  $\eta_{\text{ORR}}$  by 0.07 eV. Using the calculated over potential  $\eta_{\text{ORR}}$  for all systems enables us to construct an activity volcano plot, where the  $\Delta E_{\text{O}}$  is used as a descriptor to evaluate the catalytic activity. The results are shown in Figure 4g. The systems that are located in left side of the volcano plot are limited by the hydrogenation step, while the systems located at the right side of the volcano exhibit weaker  $\Delta E_{\text{O}}$  and as result the limiting step is the dissociation of molecular oxygen. We observe

that cs-Pt-Co-x systems with 2- and 3-shell layers exhibit lower  $\eta_{\text{ORR}}$  than pure Pt(111), thus larger catalytic activity. However, increasing the number of shell layers signify an increase of  $\Delta E_{\text{O}}$  reaching values similar to those in the bulk, and as a result the  $\eta_{\text{ORR}}$  will be similar to pure Pt(111). On the other hand, if the shell composition is similar to Pt<sub>3</sub>Co systems, with a Pt overlayer, the  $\eta_{\text{ORR}}$  will be smaller than for pure Pt(111) when the shell thickness is equal or larger than 3 metal layers, resulting in enhanced catalytic activity almost independent of the shell thickness.

As a summary, the DFT results suggest that the excellent electrocatalytic activity cannot be explained by core-shell structures having pure Pt in the outer shell, since a particle having four shells or more of pure Pt (the number of Pt-rich layers in our study is 5-6) would behave similar to bulk Pt (which do not agree with our experimental observations where the cs-Pt<sub>3</sub>Co catalyst exhibit significantly better efficiency than the pure Pt/Vulcan sample). Instead the conclusion must be that the shell of the cuboctahedral nanoparticles must have a composition similar to Pt<sub>3</sub>Co (still with one pure layer of Pt) forming a skeleton-type structure. This decreases the  $\Delta E_{\text{O}}$  improving the catalytic activity even when the shell thickness is larger than 3 metal slabs, as is in our cs-Pt<sub>3</sub>Co nanoparticles.

## Conclusions

We have reported a synthesis of highly ordered, homogeneous, cuboctahedral core-shell Pt<sub>3</sub>Co nanoparticles. By detailed

experimental characterization as well as extensive DFT calculations, we conclude that the cs-Pt<sub>3</sub>Co nanoparticles must be composed of a skin rich in Pt, a shell configuration of 5-6 layers which also is Pt-rich but need to contain also Co atoms, and finally a core, which is relatively Co-rich. Only this structure is consistent with the very high electrocatalytic activity of cs-Pt<sub>3</sub>Co with more than 6 times higher than commercial Pt/Vulcan, and 5 times more active than non-faceted alloy sp-Pt<sub>3</sub>Co nanoparticles. Our study gives important insight into the design and understanding of advanced bimetallic nanoparticles, which has both scientific and technological impact.

## Acknowledgements

This work was supported by the Artificial Leaf Project Umeå (K&A Wallenberg foundation) and by the Swedish Research Council (Grant dnr 2013-5252). G.Z.H. acknowledges support from 1000-Talent Program (Recruitment Program of Global Expert, In Chinese: Qian-Ren-Ji-Hua) and the Special Talent Foundation of Director of Xinjiang Technical Institute of Physics & Chemistry, Chinese Academy of Sciences and National Natural Science Foundation of China (21505154). E.G.E. acknowledges support from Ångpanneföreningen's Foundation (14-541). G.Y. acknowledges the funding from the National Natural Science Foundation of China (Grant No. 51202180), the Fundamental Research Funds for the Central Universities in China and the Scientific Research Foundation for the Returned Overseas Chinese Scholars, State Education Ministry. The theoretical simulations were performed on resources provided by the Swedish National Infrastructure for Computing at the High Performance Computing Center North (HPC2N). We wish to thank Qingxue Lai and Prof. Yanyu Liang at Nanjing University of Aeronautics and Astronautics for assistance with electrochemical measurements.

## Notes and references

1. J. K. Nørskov, J. Rossmeisl, A. Logadottir, L. Lindqvist, J. R. Kitchin, T. Bligaard and H. Jónsson, *The Journal of Physical Chemistry B*, 2004, **108**, 17886-17892.
2. G. Wu, K. L. More, C. M. Johnston and P. Zelenay, *Science*, 2011, **332**, 443-447.
3. C. Wang, H. Daimon, Y. Lee, J. Kim and S. Sun, *Journal of the American Chemical Society*, 2007, **129**, 6974-6975.
4. H.-W. Liang, X. Cao, F. Zhou, C.-H. Cui, W.-J. Zhang and S.-H. Yu, *Advanced Materials*, 2011, **23**, 1467-1471.
5. S. M. Alia, G. Zhang, D. Kisailus, D. Li, S. Gu, K. Jensen and Y. Yan, *Advanced Functional Materials*, 2010, **20**, 3742-3746.
6. C. N. Brodsky, A. P. Young, K. C. Ng, C. H. Kuo and C. K. Tsung, *Acs Nano*, 2014, **8**, 9368-9378.
7. B. T. Sneed, A. P. Young, D. Jalalpoor, M. C. Golden, S. J. Mao, Y. Jiang, Y. Wang and C. K. Tsung, *Acs Nano*, 2014, **8**, 7239-7250.
8. G. Hu, F. Nitze, E. Gracia-Espino, J. Ma, H. R. Barzegar, T. Sharifi, X. Jia, A. Shchukarev, L. Lu and C. Ma, *Nature communications*, 2014, **5**.
9. R. B. Gordon, M. Bertram and T. Graedel, *P Natl Acad Sci USA*, 2006, **103**, 1209-1214.
10. H. Zhu, S. Zhang, S. Guo, D. Su and S. Sun, *Journal of the American Chemical Society*, 2013, **135**, 7130-7133.
11. S. Guo, S. Zhang, X. Sun and S. Sun, *Journal of the American Chemical Society*, 2011, **133**, 15354-15357.
12. B. Y. Xia, H. B. Wu, X. Wang and X. W. Lou, *Journal of the American Chemical Society*, 2012, **134**, 13934-13937.
13. F. Hasche, M. Oezaslan and P. Strasser, *Chemcatchem*, 2011, **3**, 1805-1813.
14. M. Oezaslan, F. Hasche and P. Strasser, *Journal of the Electrochemical Society*, 2012, **159**, B444-B454.
15. M. Oezaslan, F. Hasche and P. Strasser, *Journal of the Electrochemical Society*, 2012, **159**, B394-B405.
16. C. H. Cui, L. Gan, H. H. Li, S. H. Yu, M. Heggen and P. Strasser, *Nano Lett*, 2012, **12**, 5885-5889.
17. V. R. Stamenkovic, B. Fowler, B. S. Mun, G. Wang, P. N. Ross, C. A. Lucas and N. M. Marković, *Science*, 2007, **315**, 493-497.
18. J. K. Nørskov, F. Abild-Pedersen, F. Studt and T. Bligaard, *Proceedings of the National Academy of Sciences*, 2011, **108**, 937-943.
19. V. R. Stamenkovic, B. S. Mun, M. Arenz, K. J. J. Mayrhofer, C. A. Lucas, G. Wang, P. N. Ross and N. M. Markovic, *Nat Mater*, 2007, **6**, 241-247.
20. E. Gracia-Espino, X. Jia and T. Wagberg, *Journal of Physical Chemistry C*, 2014, **118**, 2804-2811.
21. K. A. Kuttiyiel, K. Sasaki, Y. Choi, D. Su, P. Liu and R. R. Adzic, *Nano Lett*, 2012, **12**, 6266-6271.
22. V. R. Stamenkovic, B. S. Mun, K. J. J. Mayrhofer, P. N. Ross and N. M. Markovic, *Journal of the American Chemical Society*, 2006, **128**, 8813-8819.
23. W. Kohn and L. J. Sham, *Physical Review*, 1965, **140**, A1133-A1138.
24. B. Hammer, L. B. Hansen and J. K. Nørskov, *Physical Review B*, 1999, **59**, 7413-7421.
25. J. Junquera, Ó. Paz, D. Sánchez-Portal and E. Artacho, *Physical Review B*, 2001, **64**, 235111.
26. H. J. Monkhorst and J. D. Pack, *Physical Review B*, 1976, **13**, 5188-5192.
27. M. Methfessel and A. T. Paxton, *Physical Review B*, 1989, **40**, 3616-3621.
28. M. S. José, A. Emilio, D. G. Julian, G. Alberto, J. Javier, O. Pablo and S.-P. Daniel, *Journal of Physics: Condensed Matter*, 2002, **14**, 2745.
29. A. Gómez-Rodríguez, L. M. Beltrán-del-Río and R. Herrera-Becerra, *Ultramicroscopy*, 2010, **110**, 95-104.
30. M. K. Carpenter, T. E. Moylan, R. S. Kukreja, M. H. Atwan and M. M. Tessema, *Journal of the American Chemical Society*, 2012, **134**, 8535-8542.
31. F. Gloaguen, J. M. Le'Ger and C. Lamy, *Journal of Applied Electrochemistry*, 1997, **27**, 1052-1060.
32. J. Xiao, Q. Kuang, S. Yang, F. Xiao, S. Wang and L. Guo, *Sci. Rep.*, 2013, **3**.
33. J. P. Collman, L. Fu, P. C. Herrmann and X. Zhang, *Science*, 1997, **275**, 949-951.
34. W. P. Davey, *Physical Review*, 1925, **25**, 753-761.
35. J. Greeley and J. K. Nørskov, *The Journal of Physical Chemistry C*, 2009, **113**, 4932-4939.
36. P. Strasser, S. Koh, T. Anniyev, J. Greeley, K. More, C. Yu, Z. Liu, S. Kaya, D. Nordlund, H. Ogasawara, M. F. Toney and A. Nilsson, *Nat Chem*, 2010, **2**, 454-460.

## Table of content

A detailed experimental study on the origin of the High Oxygen Reduction Electrocatalytic Activity of Cuboctahedral Pt<sub>3</sub>Co-Pt Core-Shell Nanoparticles is presented.

